TU Delft

Delft University of Technology

Singlet and triplet Cooper pair splitting in hybrid superconducting nanowires

Wang, Guanzhong; Dvir, Tom; Mazur, Grzegorz P.; Liu, Chun Xiao; van Loo, Nick; ten Haaf, Sebastiaan L.D.; Bordin, Alberto; Gazibegovic, Sasa; Badawy, Ghada; Bakkers, Erik P.A.M.

DOI
10.1038/s41586-022-05352-2

Publication date
2022

Document Version
Final published version

Published in
Nature

Citation (APA)
Wang, G., Dvir, T., Mazur, G. P., Liu, C. X., van Loo, N., ten Haaf, S. L. D., Bordin, A., Gazibegovic, S., Badawy, G., Bakkers, E. P. A. M., Wimmer, M., & Kouwenhoven, L. P. (2022). Singlet and triplet Cooper pair splitting in hybrid superconducting nanowires. *Nature*, *612*(7940), 448-453. https://doi.org/10.1038/s41586-022-05352-2

Important note
To cite this publication, please use the final published version (if applicable).
Please check the document version above.

Copyright
Other than for strictly personal use, it is not permitted to download, forward or distribute the text or part of it, without the consent of the author(s) and/or copyright holder(s), unless the work is under an open content license such as Creative Commons.

Takedown policy
Please contact us and provide details if you believe this document breaches copyrights.
We will remove access to the work immediately and investigate your claim.

This work is downloaded from Delft University of Technology.
For technical reasons the number of authors shown on this cover page is limited to a maximum of 10.

Green Open Access added to TU Delft Institutional Repository

'You share, we take care!' - Taverne project

https://www.openaccess.nl/en/you-share-we-take-care

Otherwise as indicated in the copyright section: the publisher is the copyright holder of this work and the author uses the Dutch legislation to make this work public.

Singlet and triplet Cooper pair splitting in hybrid superconducting nanowires

https://doi.org/10.1038/s41586-022-05352-2

Received: 17 May 2022

Accepted: 15 September 2022

Published online: 23 November 2022

Check for updates

Guanzhong Wang[1,3], Tom Dvir[1,3]✉, Grzegorz P. Mazur[1,3], Chun-Xiao Liu[1], Nick van Loo[1], Sebastiaan L. D. ten Haaf[1], Alberto Bordin[1], Sasa Gazibegovic[2], Ghada Badawy[2], Erik P. A. M. Bakkers[2], Michael Wimmer[1] & Leo P. Kouwenhoven[1]

In most naturally occurring superconductors, electrons with opposite spins form Cooper pairs. This includes both conventional *s*-wave superconductors such as aluminium, as well as high-transition-temperature, *d*-wave superconductors. Materials with intrinsic *p*-wave superconductivity, hosting Cooper pairs made of equal-spin electrons, have not been conclusively identified, nor synthesized, despite promising progress[1–3]. Instead, engineered platforms where *s*-wave superconductors are brought into contact with magnetic materials have shown convincing signatures of equal-spin pairing[4–6]. Here we directly measure equal-spin pairing between spin-polarized quantum dots. This pairing is proximity-induced from an *s*-wave superconductor into a semiconducting nanowire with strong spin–orbit interaction. We demonstrate such pairing by showing that breaking a Cooper pair can result in two electrons with equal spin polarization. Our results demonstrate controllable detection of singlet and triplet pairing between the quantum dots. Achieving such triplet pairing in a sequence of quantum dots will be required for realizing an artificial Kitaev chain[7–9].

To probe spin pairing, one can split up a Cooper pair, separate the two electrons and measure their spins. The process to split a Cooper pair is known as crossed Andreev reflection (CAR)[10–12]. In this process, the two electrons end up in two separated non-superconducting probes (Fig. 1a), each of these normal (N) probes collecting a single elementary charge, *e*. Alternative processes exist such as normal Andreev reflection (AR), with a 2*e* charge exchange between a single normal probe and the superconductor (S), and elastic co-tunnelling (ECT), with 1*e* charge from one normal probe crossing the superconductor and ending up in the other normal probe. AR does not enable measurement of the separate spins and thus this process needs to be suppressed. Following the approach of previous Cooper pair-splitting studies[13–18], we realize this by using quantum dots (QDs) with large charging energies that only allow for 1*e* transitions. This suppresses 2*e* AR to approximately 5% of the total current in each junction (see Extended Data Fig. 2). The remaining CAR and ECT processes are sketched in Fig. 1b. In ECT, 1*e* is subtracted from one QD and added to the other, whereas in CAR, an equal-sign 1*e* charge is either added or subtracted simultaneously to each QD. We will use this difference to distinguish ECT from CAR. Besides charge detection, QDs can be configured to be spin-selective in a magnetic field[19,20]. Figure 1c illustrates that ECT involves equal spin states in both QDs, whereas CAR from a singlet Cooper pair requires opposite spin states. Interestingly, these rules of spin combinations can be relaxed in the presence of inhomogeneous magnetic fields or spin–orbit interaction, both of which allow the possibility of triplet pairing[21–29]. For instance, spin–orbit coupling (SOC) can rotate an opposite-spin configuration into an equal-spin pair. In this report, we first demonstrate charge measurements, as illustrated in Fig. 1b, followed by spin-selective detection of ECT and CAR, which sets us up to detect CAR with equal spins when spin precessions are induced by SOC.

Charge filtering

The device and the measurement set-up are illustrated in Fig. 1d. A short segment of an InSb nanowire is proximitized by a thin Al shell, which is kept grounded throughout the experiment. Two QDs are formed on both sides of the hybrid segment. The electrochemical potentials in the two QDs, μ_{LD} and μ_{RD}, are controlled by voltages on the respective gates, V_{LD} and V_{RD}. Crucially, the level spacing between QD orbitals exceeds 1 meV, such that near each charge degeneracy the QD can be considered as a single orbital level. Two normal leads (Au) are attached to both QDs. Both leads are independently voltage biased (V_L, V_R), and the currents through the leads are measured separately (I_L, I_R).

The energy diagram in Fig. 1e illustrates that ECT requires alignment of the QD levels ($\mu_{LD} = \mu_{RD}$), both positioned within the transport window defined by the bias voltages V_L and V_R. We restrict the bias settings to $V_L = -V_R$ for ECT unless mentioned otherwise. In Fig. 1e, the transport window is thus defined by $-eV_L > \mu_{LD} = \mu_{RD} > -eV_R$. To study co-tunnelling processes that only occupy a higher-energy intermediary state virtually, the QD excitations and bias voltages are kept within the induced superconducting gap, that is, lower in energy than any state in the hybrid (see Extended Data Fig. 9). We define current to be positive when flowing from N to S for both sides, implying that ECT yields opposite currents, $I_L = -I_R$. On the other hand, CAR requires anti-symmetric alignment between the two QD levels, $\mu_{LD} = -\mu_{RD}$ (ref. [17]), to satisfy overall energy conservation, as shown in Fig. 1f. We restrict bias settings to $V_L = V_R$ for CAR unless specified. Thus, the transport window in Fig. 1f is

[1]QuTech and Kavli Institute of NanoScience, Delft University of Technology, Delft, The Netherlands. [2]Department of Applied Physics, Eindhoven University of Technology, Eindhoven, The Netherlands. [3]These authors contributed equally: Guanzhong Wang, Tom Dvir and Grzegorz P. Mazur. ✉e-mail: tom.dvir@gmail.com

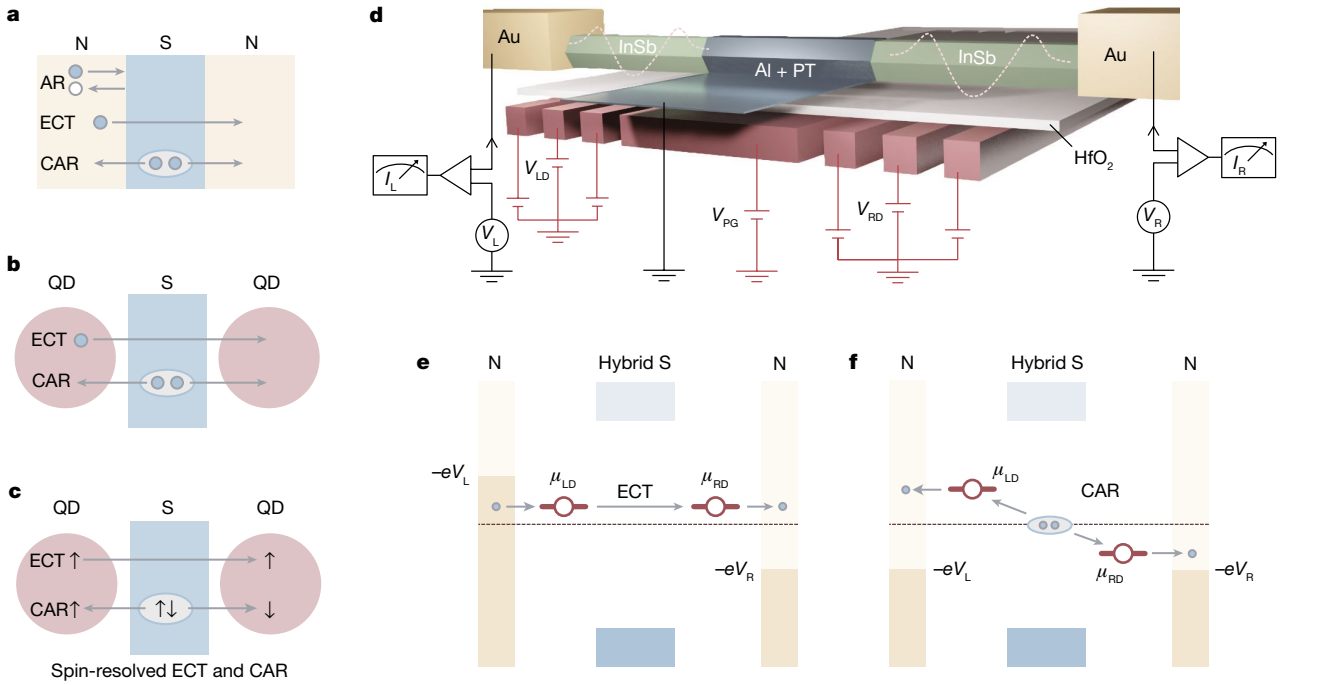

Fig. 1 | Transport processes, device and energy diagrams. a, Possible electron transport processes in a normal–superconductor–normal (N–S–N) structure: local Andreev reflection (AR), elastic co-tunnelling (ECT) and crossed Andreev reflection (CAR). **b**, A QD–S–QD structure enables only ECT and CAR. **c**, The QDs become spin-selective in a magnetic field, allowing us to distinguish ECT between equal spin states and CAR from a singlet Cooper pair involving opposite spins. **d**, Illustration of the N–QD–S–QD–N device and the measurement circuit. Dashed potentials indicate QDs defined in the nanowire by finger gates. **e**,**f**, Energy diagrams for ECT (**e**) and CAR (**f**) with detection by varying bias voltages and QD energy alignments. Occupied (unoccupied) states are illustrated by darker (lighter) colours.

now defined by $-eV_L = -eV_R < \mu_{LD} = -\mu_{RD} < eV_L = eV_R$, allowing tunnelling from the QDs into empty states in the nearby leads. In our definition the CAR-induced currents are equal: $I_L = I_R$. The boundaries of the transport window are further illustrated in Fig. 2b,c.

A scanning electron microscope image of the main device, A, is shown in Fig. 2a. In Fig. 2d we show I_L and I_R as functions of the two QD voltages for fixed $V_L = -V_R = 100$ μV. The two currents are close to the expected $I_L = -I_R$ (see also Extended Data Fig. 2) and are strong along a straight line with a positive slope. Using the lever arm of QD gates extracted in Extended Data Fig. 1, we find this line to be $\mu_{LD} = \mu_{RD}$. In Fig. 2e, we set $V_L = V_R = 150$ μV and similarly observe $I_L \approx I_R$ along a straight line with a negative slope where $\mu_{LD} = -\mu_{RD}$. Several features in these data allow us to attribute the origin of these subgap currents to CAR and ECT instead of competing transport processes. The nonlocal origin of the measured currents, expressed by the (anti-)symmetric energy requirement on both QDs and current correlation, rules out local Andreev reflection. The bias and QD energies being kept lower than any subgap bound state excludes resonant tunnelling into and out of them. The only mechanisms known to us that can explain these observations are CAR and ECT[30].

In Extended Data Fig. 2 we extract from this measurement Cooper pair splitting visibilities of 91% and 98% for the left and right QDs, respectively. Their product of 90%, to our knowledge realized for the first time, exceeds the minimum value of 71% required for a Bell test[16]. The high efficiency of Cooper pair splitting reported in this work compared to previous reports relies on having a hard superconducting gap in the proximitized segment and on having multiple gates for each QD, allowing control of the chemical potential of QDs independently from QD–lead couplings. Both requirements are enabled by recent advancements in the fabrication technique[31]. The dashed lines in Fig. 2d,e indicate the boundaries of the transport window, as illustrated with corresponding colours surrounding the grey area in Fig. 2b,c. For convenience, we introduce the correlated current $I_{corr} \equiv \mathrm{sgn}(I_L I_R)\sqrt{|I_L I_R|}$, plotted in Fig. 2f,g for the corresponding ECT and CAR measurements. This product is finite only when currents through both junctions are nonzero, allowing us to focus on features produced by ECT or CAR (see Extended Data Fig. 10). Its sign directly reflects the dominant process: ECT being negative and CAR positive.

Spin blockade at zero magnetic field

Spin-degenerate orbital levels can each be occupied with two electrons with opposite spins. Figure 3a shows the charge stability diagram measured with negative biases on both N leads. We label the charge occupations relative to the lower-left corner, with some unknown but even number of electrons in each QD. Increasing the gate voltages V_{LD} and V_{RD} increases the occupation of left and right QD levels one by one from (0, 0) to (2, 2). In between charge transitions, the occupation is fixed with possible spin configurations as indicated in Fig. 3a. At charge degeneracies, I_{corr} is generally nonzero. However, the correlated current is very weak at the (0, 0) ↔ (1, 1) transition compared to the other three. This can be understood as a CAR-mediated spin-blockade, illustrated in Fig. 3b. At the (0, 0) ↔ (1, 1) transition, each QD can receive an electron with any random spin orientation from the leads. Opposite spins can recombine into a Cooper pair. However, whenever the QDs are both occupied with the same spin, CAR is suppressed and thereby blocks the transport cycle. Note that SOC in InSb is known to not lift this blockade[32,33]. Figure 3c also shows a similar ECT-mediated spin blockade when applying anti-symmetric biases to the N leads. This effect is intimately related to the well-known Pauli spin blockade in double QDs[34–36] and shows that spins are well defined and relax slowly compared to the transport cycle time (a few nanoseconds for currents on the order of 100 pA). Figure 3c shows CAR and ECT for all

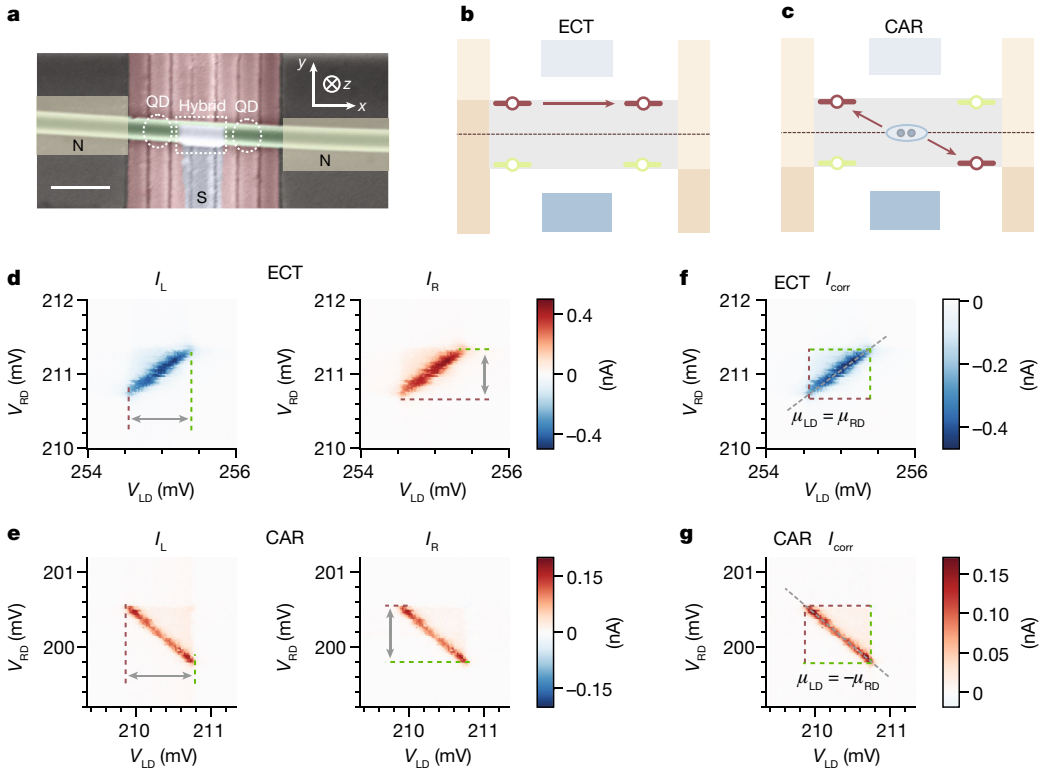

Fig. 2 | CAR and ECT. a, False-colour SEM image of device A prior to the fabrication of normal (N) leads, using the same colour representation as in Fig. 1d. Translucent rectangles indicate locations of N leads. Dotted lines indicate QDs and the hybrid segment in the middle. Scale bar is 300 nm. Inset, our coordinate system. The nanowire lies at a 3° angle to the *x* axis. **b**,**c**, Energy diagrams for ECT (**b**) and CAR (**c**) measurements. The grey areas bound by bias voltages indicate the transport window. The QD levels represent two possible scenarios of energy alignment at the boundaries of the transport window (brown and green). **d**, Measured I_L and I_R for the bias configuration illustrated in **b**, which selects for ECT. Dashed lines mark the transport window boundaries using the same colours as QD illustrations in **b**. Data were taken with $B_x = 0.1$ T and $V_{PG} = 0.18$ V. **e**, Measured I_L and I_R for the bias configuration illustrated in **c**, which selects for CAR. **f**, The correlated current, I_{corr}, through the two QDs calculated from data in **d**. The dashed box marks the transport window, and the diagonal dashed line indicates where the QD levels are aligned. **g**, As in **f**, for data from **e**. Here the diagonal dashed line indicates where the QD levels are anti-aligned.

four bias–polarity combinations. In each of them, one out of the four joint charge degeneracy points exhibits suppressed current. The spin configurations that lead to blockade are sketched in Fig. 3d. To sum up the general principle, ECT cannot occur if an electron of a certain spin needs to tunnel into an orbital already occupied with the same spin. On the other hand, CAR cannot proceed if Cooper pairs must be split into or combined from an equal-spin occupation of the two dots. Similar to double QDs, we believe that the residual current under blockade conditions is due to hyperfine interaction[33].

Spin filtering

At finite magnetic field B, the four charge degeneracies in Fig. 3a can become bipolar spin filters[19,20]. This requires the Zeeman energy in the QDs to exceed the bias voltage, electron temperature and hyperfine interaction, yet remain smaller than the level spacing of the QDs. Under these conditions, we use ↑/↓ (along the applied B direction) to denote the two spin-split QD eigenstates. Only ↓ electrons are transported across a QD at the $0 \leftrightarrow 1$ transition and only ↑ electrons at $1 \leftrightarrow 2$. Figure 4b illustrates the consequence of spin-filtering for CAR processes, namely a complete suppression for parallel spins. The opposite is expected for ECT with only spin-conserved tunnelling allowed. We first apply $B = B_y = 100$ mT, in the plane of the substrate and perpendicular to the nanowire. The four panels in Fig. 4c present I_{corr} measured at four bias polarity combinations, selecting either CAR or ECT conditions. The upper right panel also shows the lowest-energy spin combinations. I_{corr} vanishes for ↑↑ and ↓↓ with CAR biases −− and ++, and for ↑↓ and ↓↑ with ECT biases +− and −+. The observation of spin conservation suggests spin is a good quantum number. Thus, any spin–orbit field in the InSb nanowire, B_{SO} (including both possible Rashba and Dresselhaus SOC), must be parallel, or nearly parallel, to B_y. In this case, CAR provides a coupling mechanism only for an opposite-spin configuration in the two QDs. We note that the exact B_{SO} direction as measured by suppression of equal-spin CAR or opposite-spin ECT depends on gate settings and the device used (see for example, Extended Data Fig. 6). We have measured directions within 20° of being perpendicular to the nanowire axis but its angle with the substrate plane can range from 0 to 60°. This observation is consistent with the expectation of B_{SO} being perpendicular to the nanowire axis for both Rashba and Dresselhaus SOC[36–38].

To quantify the observation that CAR is anti-correlated with the spin alignment of the QDs, we perform a spin correlation analysis[39,40] similar to that in ref. [41], which analogously reports reduced CAR amplitudes when QD spins are parallel compared to anti-parallel. The results, presented in Extended Data Fig. 8, show the two QD spins are anti-correlated by a factor of −0.86 for CAR signals when pairing is singlet, to our knowledge the highest reported so far.

When we apply $B \perp B_{SO}$, in a classical analogy, the spin–orbit interaction leads to spin precession about the B_{SO} axis in the hybrid section while the QDs remain approximately polarized along B (refs. [36,42]; see Supplementary Information for detailed discussions). Now, an injected ↑ electron can acquire a finite ↓ component and combine with another ↑

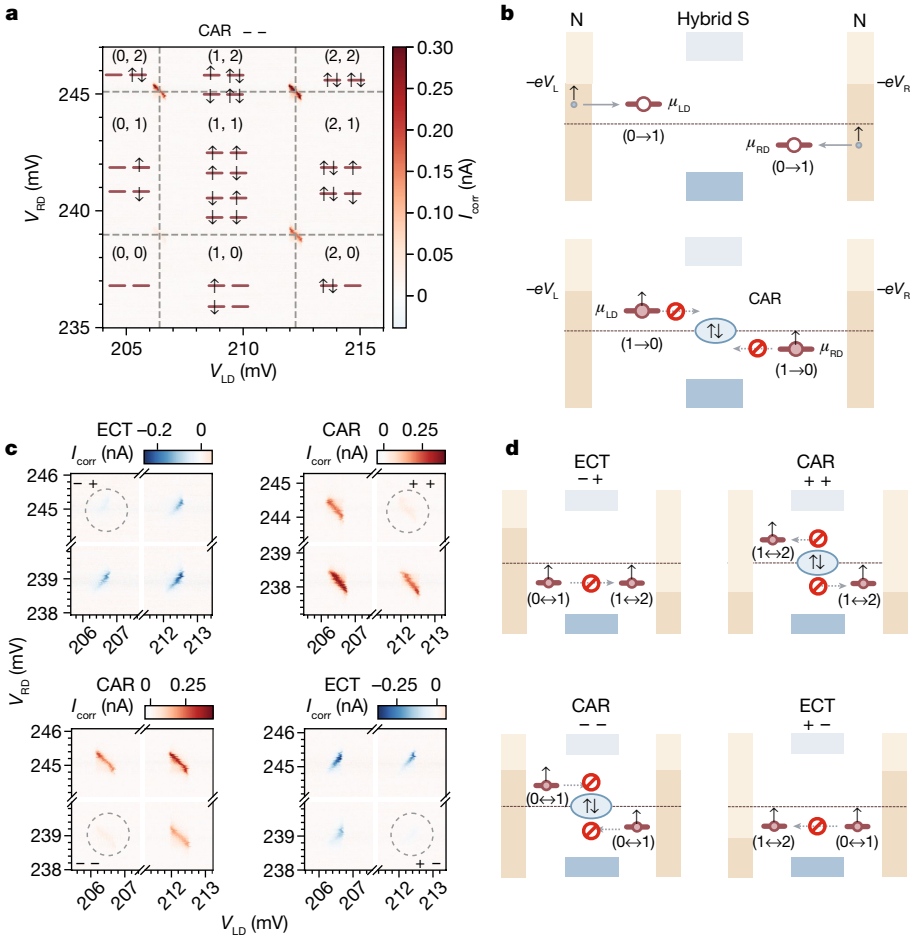

Fig. 3 | Spin blockade of CAR and ECT at zero magnetic field. a, Charge stability diagram of the two QDs coupled via the hybrid section. I_{corr} is measured with −100 μV biases on both N leads (denoted – –), that is, under CAR conditions. The shown region in gate space covers four charge degeneracy points. **b**, Illustration of CAR-mediated spin blockade. Small arrows indicate the spin polarization of the electrons participating in the transport. **c**, I_{corr} under all four combinations of bias polarities (–+, ++, +–, ––, in clockwise order from top left). Axes are interrupted in the Coulomb-blockaded range to allow for magnification of the charge transitions. Grey dashed circles indicate conditions for either ECT-mediated or CAR-mediated spin blockade. **d**, Illustration of spin-blockade conditions with bias configurations corresponding to the four panels in **c**. The QD occupations through a complete cycle are indicated.

electron into a Cooper pair, as illustrated in Fig. 4e. Similarly, spin precession generates a nonzero probability of coupling opposite spins via ECT. These expectations are indeed confirmed in Fig. 4f. We again use biases to select ECT or CAR for the four spin-polarized charge degeneracy points. Notably, faint but finite CAR signals appear in ↑↑ and ↓↓ spin combinations (highlighted by dashed circles), as well as for ↑↓ and ↓↑ in ECT. The observed CAR coupling for ↑↑ and ↓↓ is interpreted as a measure of the equal-spin coupling between the QDs. In Extended Data Fig. 4, we show that these observations do not qualitatively depend on the magnitude of $|B|$ as long as spin polarization is complete (above approximately 50 mT).

To further investigate the field-angle dependence, we measure CAR and ECT while rotating $|B| = 100$ mT in the plane of the substrate, see Fig. 4g. For this measurement, we apply a ±100 μV bias voltage only on one side of the device, while keeping the other bias zero. This enables us to measure both CAR and ECT without changing the applied biases, as can be understood from the same basic principles outlined in Fig. 1 (see Extended Data Fig. 6 for details of this measurement scheme, and the associated data repository (see section 'Data availability') for plots of the raw data). We take the maximum value of each I_{corr} scan at a particular bias and spin combination as the CAR magnitude and the absolute value of the minimum for ECT. Along the two directions parallel to B_{SO}, $\varphi \approx 90°$ and 270°, equal-spin CAR and opposite-spin ECT are forbidden. (The finite extracted amplitudes in this dataset are our noise floor, although small amounts of equal-spin CAR and opposite-spin ECT even when $B \parallel B_{SO}$ can also be observed in other datasets such as Extended Data Fig. 6.) When $B \perp B_{SO}$ (that is, $\varphi \approx 0°$ and 180°) the anomalous signals are the largest, as expected for effects caused by spin–orbit interaction[36,38]. The signals corresponding to favoured spin combinations (for example, ↑↓ CAR) do not always exhibit as clear oscillations for reasons we do not yet understand.

Discussion

The oscillating CAR signals in Fig. 4g for the two equal-spin configurations (leftmost and rightmost panels) are the central results of this work. The presence of the anomalous equal-spin CAR signal shows how non-collinear B and B_{SO} leads to unconventional spin pairing between QDs. Below we discuss possible microscopic scenarios giving rise to SOC-induced spin precession. InSb nanowires have both Rashba-type and Dresselhaus-type SOC. Both terms are linear in the momentum along the nanowire axis and their addition gives an effective spin–orbit term in a direction generally perpendicular to the nanowire axis [38]. Such SOC also exists in our InSb-based QDs and can lead to nominally ↑ QD eigenstates having a small ↓ component[43]. In Extended Data Fig. 3 and Supplementary Information, we quantify this effect and argue that the

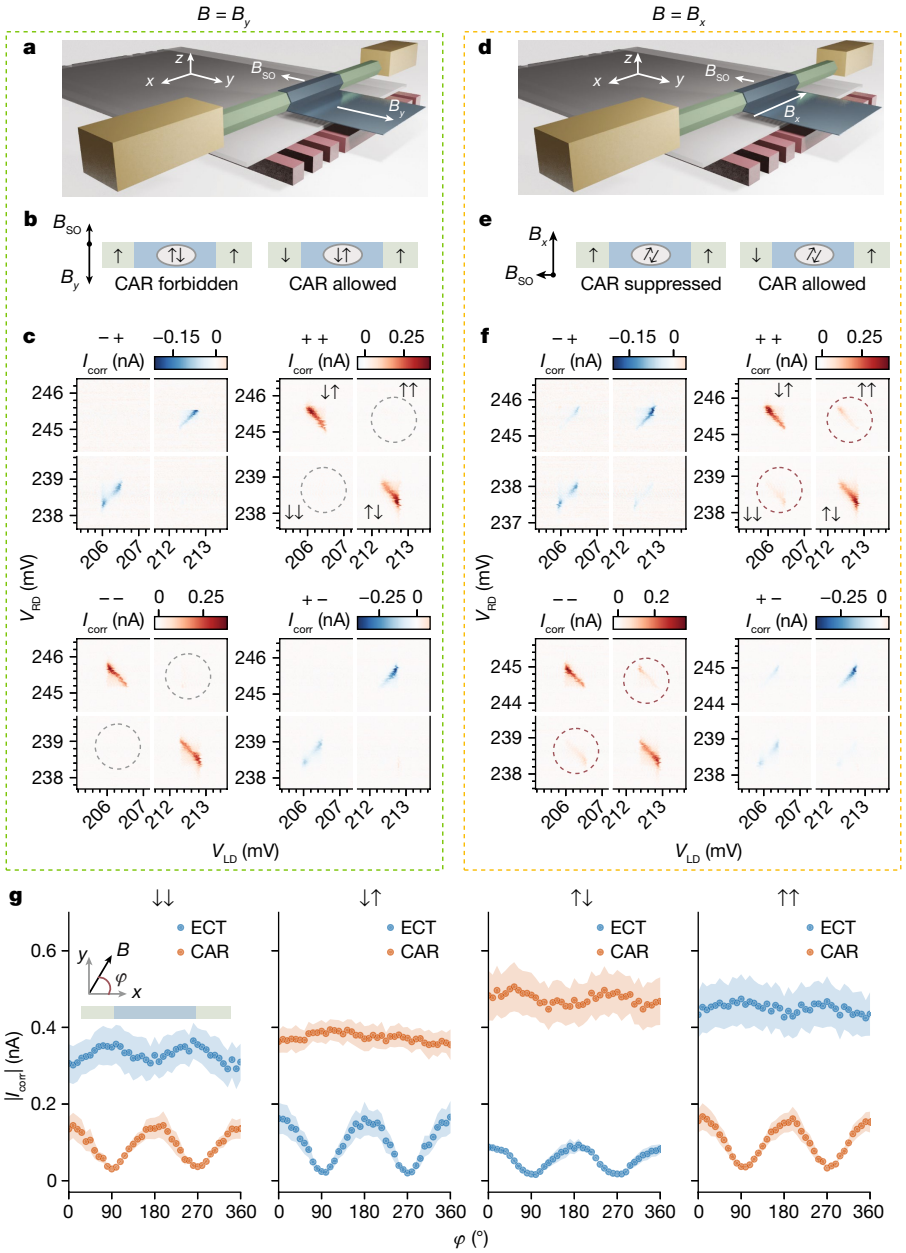

Fig. 4 | Spin-resolved CAR and ECT. a, Illustration of the externally applied B direction relative to the nanowire axis for **b** and **c**. In all illustrations, notations ↑ and ↓ are defined along the applied B direction. **b**, Illustration of allowed and forbidden CAR when $B \parallel B_{SO}$. **c**, I_{corr} under the four bias and four spin combinations in the two QDs for $B \parallel B_{SO}$ and $B = B_y = 100$ mT. Vanishing CAR currents due to QD spin-filtering are indicated with dashed circles. **d**, Illustration of the B direction for **e** and **f**. **e**, Illustration of spin-filtering when $B \perp B_{SO}$. **f**. Similar to **c**, but for $B = B_x \perp B_{SO}$. CAR currents that result from equal-spin Cooper pair splitting are circled in red. **g**, I_{corr} for four QD spin combinations versus the angle of the in-plane magnetic field. Each data point is the mean of all four bias configurations ($V_{L,R} = \pm 100\mu V$, see main text) and the error bars show the 1σ spread. Inset, the direction of B relative to the nanowire.

opposite-spin admixture is too small to explain the measured amplitude of the ECT and CAR anisotropy.

The superconducting pairing in the hybrid segment itself is predicted to hold a triplet component owing to SOC as well[44]. The shape and amplitude of our observed oscillations allow comparison with a theory adopting this assumption[45], resulting in an estimated spin–orbit strength in the hybrid section between 0.11 and 0.18 eV Å for device A and 0.05 to 0.07 eV Å for device B (see Extended Data Fig. 5). This estimation agrees with reported values in the literature[46,47]. Although the existence of triplet pairing component in the hybrid is thus consistent with our results, it is not the only possible explanation. During the tunnelling process between the QDs, the electrons traverse through a bare InSb segment, the SOC of which could also result in spin precession[36,38]. Both scenarios, however, support an interpretation of spin-triplet superconducting coupling between the QDs necessary for construction of a Kitaev chain[8].

Finally, we remark that the role of the middle Al–InSb hybrid segment of our devices in electron transport has not been discussed in this work. Extended Data Fig. 9 shows that this segment hosts discrete Andreev bound states owing to strong confinement in all three dimensions and these states are tunnel-coupled to both N leads. The parallel theoretical work modelling this experiment[45] shows that these states are expected to strongly influence CAR and ECT processes upon variation of the gate voltage underneath the hybrid segment. The experimental

observations of the gate tunability of CAR and ECT will be presented in a future manuscript (A.B. et al., manuscript in preparation).

Conclusion

In conclusion, we have measured CAR and ECT in an N–QD–S–QD–N device with and without spin-filtering. For well-defined, specific settings consistent with our expectations, we observe Cooper pair splitting for equal spin states in the QD probes. These observations are consistent with the presence of a triplet component in the superconducting pairing in the proximitized nanowires, which is one of the building blocks for a topological superconducting phase[48,49]. More generally, our results show that the combination of superconductivity and SOC can generate triplet CAR between spin-polarized QDs, paving the road to an artificial Kitaev chain[7–9]. The realization of a Kitaev chain further requires increasing the coupling strength between QDs to allow the formation of a hybridized, extended state. This is confirmed in a parallel work where the QDs are driven to the strong coupling regime[50].

Online content

Any methods, additional references, Nature Portfolio reporting summaries, source data, extended data, supplementary information, acknowledgements, peer review information; details of author contributions and competing interests; and statements of data and code availability are available at https://doi.org/10.1038/s41586-022-05352-2.

1. Ran, S. et al. Nearly ferromagnetic spin-triplet superconductivity. *Science* **365**, 684–687 (2019).
2. Zhou, H., Xie, T., Taniguchi, T., Watanabe, K. & Young, A. F. Superconductivity in rhombohedral trilayer graphene. *Nature* **598**, 434–438 (2021).
3. Zhou, H. et al. Isospin magnetism and spin-polarized superconductivity in Bernal bilayer graphene. *Science* **375**, 774–778 (2022).
4. Robinson, J., Witt, J. & Blamire, M. Controlled injection of spin-triplet supercurrents into a strong ferromagnet. *Science* **329**, 59–61 (2010).
5. Khaire, T. S., Khasawneh, M. A., Pratt, W. P. & Birge, N. O. Observation of spin-triplet superconductivity in co-based Josephson junctions. *Phys. Rev. Lett.* **104**, 137002 (2010).
6. Sprungmann, D., Westerholt, K., Zabel, H., Weides, M. & Kohlstedt, H. Evidence for triplet superconductivity in Josephson junctions with barriers of the ferromagnetic Heusler alloy Cu_2MnAl. *Phys. Rev. B* **82**, 060505 (2010).
7. Kitaev, A. Y. Unpaired Majorana fermions in quantum wires. *Phys.-Usp.* **44**, 131–136 (2001).
8. Sau, J. D. & Sarma, S. D. Realizing a robust practical Majorana chain in a quantum-dot–superconductor linear array. *Nat. Commun.* **3**, 964 (2012).
9. Leijnse, M. & Flensberg, K. Parity qubits and poor man's Majorana bound states in double quantum dots. *Phys. Rev. B* **86**, 134528 (2012).
10. Beckmann, D., Weber, H. & Löhneysen, H. V. Evidence for crossed Andreev reflection in superconductor–ferromagnet hybrid structures. *Phys. Rev. Lett.* **93**, 197003 (2004).
11. Russo, S., Kroug, M., Klapwijk, T. M. & Morpurgo, A. F. Experimental observation of bias-dependent nonlocal Andreev reflection. *Phys. Rev. Lett.* **95**, 027002 (2005).
12. Recher, P., Sukhorukov, E. V. & Loss, D. Andreev tunneling, coulomb blockade, and resonant transport of nonlocal spin-entangled electrons. *Phys. Rev. B* **63**, 165314 (2001).
13. Hofstetter, L., Csonka, S., Nygård, J. & Schönenberger, C. Cooper pair splitter realized in a two-quantum-dot Y-junction. *Nature* **461**, 960–963 (2009).
14. Herrmann, L. G. et al. Carbon nanotubes as Cooper-pair beam splitters. *Phys. Rev. Lett.* **104**, 026801 (2010).
15. Das, A. et al. High-efficiency Cooper pair splitting demonstrated by two-particle conductance resonance and positive noise cross-correlation. *Nat. Commun.* **3**, 1165 (2012).
16. Schindele, J., Baumgartner, A. & Schönenberger, C. Near-unity Cooper pair splitting efficiency. *Phys. Rev. Lett.* **109**, 157002 (2012).
17. Tan, Z. B. et al. Cooper pair splitting by means of graphene quantum dots. *Phys. Rev. Lett.* **114**, 096602 (2015).
18. Borzenets, I. et al. High efficiency CVD graphene–lead (Pb) Cooper pair splitter. *Sci. Rep.* **6**, 23051 (2016).
19. Recher, P., Sukhorukov, E. V. & Loss, D. Quantum dot as spin filter and spin memory. *Phys. Rev. Lett.* **85**, 1962–1965 (2000).
20. Hanson, R. et al. Semiconductor few-electron quantum dot operated as a bipolar spin filter. *Phys. Rev. B* **70**, 241304 (2004).
21. Gor'kov, L. P. & Rashba, E. I. Superconducting 2D system with lifted spin degeneracy: mixed singlet-triplet state. *Phys. Rev. Lett.* **87**, 037004 (2001).
22. Annunziata, G., Manske, D. & Linder, J. Proximity effect with noncentrosymmetric superconductors. *Phys. Rev. B* **86**, 174514 (2012).
23. Bergeret, F. S. & Tokatly, I. V. Spin–orbit coupling as a source of long-range triplet proximity effect in superconductor–ferromagnet hybrid structures. *Phys. Rev. B* **89**, 134517 (2014).
24. Linder, J. & Robinson, J. W. A. Superconducting spintronics. *Nat. Phys.* **11**, 307–315 (2015).
25. Banerjee, N. et al. Controlling the superconducting transition by spin–orbit coupling. *Phys. Rev. B* **97**, 184521 (2018).
26. Jeon, K.-R. et al. Tunable pure spin supercurrents and the demonstration of their gateability in a spin-wave device. *Phys. Rev. X* **10**, 031020 (2020).
27. Cai, R. et al. Evidence for anisotropic spin-triplet Andreev reflection at the 2D van der Waals ferromagnet/superconductor interface. *Nat. Commun.* **12**, 6725 (2021).
28. Ahmad, H. G. et al. Coexistence and tuning of spin-singlet and triplet transport in spin-filter Josephson junctions. *Commun. Phys.* **5**, 2 (2022).
29. Phan, D. et al. Detecting induced $p \pm ip$ pairing at the Al–InAs interface with a quantum microwave circuit. *Phys. Rev. Lett.* **128**, 107701 (2022).
30. Kleine, A., Baumgartner, A., Trbovic, J. & Schönenberger, C. Contact resistance dependence of crossed Andreev reflection. *Europhys. Lett.* **87**, 27011 (2009).
31. Heedt, S. et al. Shadow-wall lithography of ballistic superconductor–semiconductor quantum devices. *Nat. Commun.* **12**, 4914 (2021).
32. Danon, J. & Nazarov, Y. V. Pauli spin blockade in the presence of strong spin–orbit coupling. *Phys. Rev. B* **80**, 041301 (2009).
33. Nadj-Perge, S. et al. Disentangling the effects of spin–orbit and hyperfine interactions on spin blockade. *Phys. Rev. B* **81**, 201305 (2010).
34. Ono, K., Austing, D. G., Tokura, Y. & Tarucha, S. Current rectification by Pauli exclusion in a weakly coupled double quantum dot system. *Science* **297**, 1313–1317 (2002).
35. Hanson, R., Kouwenhoven, L. P., Petta, J. R., Tarucha, S. & Vandersypen, L. M. K. Spins in few-electron quantum dots. *Rev. Mod. Phys.* **79**, 1217–1265 (2007).
36. Hofmann, A. et al. Anisotropy and suppression of spin–orbit interaction in a GaAs double quantum dot. *Phys. Rev. Lett.* **119**, 176807 (2017).
37. Nadj-Perge, S., Frolov, S. M., Bakkers, E. Pa. M. & Kouwenhoven, L. P. Spin–orbit qubit in a semiconductor nanowire. *Nature* **468**, 1084–1087 (2010).
38. Wang, J.-Y. et al. Anisotropic Pauli spin-blockade effect and spin–orbit interaction field in an InAs nanowire double quantum dot. *Nano Letters* **18**, 4741–4747 (2018).
39. Braunecker, B., Burset, P. & Levy Yeyati, A. Entanglement detection from conductance measurements in carbon nanotube Cooper pair splitters. *Phys. Rev. Lett.* **111**, 136806 (2013).
40. Busz, P., Tomaszewski, D. & Martinek, J. Spin correlation and entanglement detection in Cooper pair splitters by current measurements using magnetic detectors. *Phys. Rev. B* **96**, 064520 (2017).
41. Bordoloi, A., Zannier, V., Sorba, L., Schönenberger, C. & Baumgartner, A. Spin cross-correlation experiments in an electron entangler. Preprint at https://arxiv.org/abs/2203.07970 (2022).
42. Stano, P. & Fabian, J. Spin–orbit effects in single-electron states in coupled quantum dots. *Phys. Rev. B* **72**, 155410 (2005).
43. Nadj-Perge, S. et al. Spectroscopy of spin–orbit quantum bits in indium antimonide nanowires. *Phys. Rev. Lett.* **108**, 166801 (2012).
44. Alicea, J. Majorana fermions in a tunable semiconductor device. *Phys. Rev. B* **81**, 125318 (2010).
45. Liu, C.-X., Wang, G., Dvir, T. & Wimmer, M. Tunable superconducting coupling of quantum dots via Andreev bound states. Preprint at https://arxiv.org/abs/2203.00107 (2022).
46. De Moor, M. W. et al. Electric field tunable superconductor–semiconductor coupling in Majorana nanowires. *New J. Phys.* **20**, 103049 (2018).
47. Bommer, J. D. S. et al. Spin–orbit protection of induced superconductivity in Majorana nanowires. *Phys. Rev. Lett.* **122**, 187702 (2019).
48. Lutchyn, R. M., Sau, J. D. & Das Sarma, S. Majorana fermions and a topological phase transition in semiconductor–superconductor heterostructures. *Phys. Rev. Lett.* **105**, 077001 (2010).
49. Oreg, Y., Refael, G. & von Oppen, F. Helical liquids and Majorana bound states in quantum wires. *Phys. Rev. Lett.* **105**, 177002 (2010).
50. Dvir, T. et al. Realization of a minimal Kitaev chain in coupled quantum dots. Preprint at https://arxiv.org/abs/2206.08045 (2022).

Publisher's note Springer Nature remains neutral with regard to jurisdictional claims in published maps and institutional affiliations.

Springer Nature or its licensor holds exclusive rights to this article under a publishing agreement with the author(s) or other rightsholder(s); author self-archiving of the accepted manuscript version of this article is solely governed by the terms of such publishing agreement and applicable law.

© The Author(s), under exclusive licence to Springer Nature Limited 2022

Methods

Device characterization and set-up

The main device, A, and the measurement set-up are illustrated in Fig. 1d. An InSb nanowire is in ohmic contact with two Cr/Au normal leads. The centre is covered with a 200-nm-wide thin Al film. Device A has 2-Å, sub-monolayer Pt grown on top, which increases the magnetic field compatibility[51]. Device B, presented in Extended Figs. 6, 7 has no Pt top layer and has a 350-nm-wide middle hybrid segment. The Al superconducting lead both proximitizes and grounds the hybrid nanowire segment. The two N leads are independently voltage-biased (V_L, V_R) and the currents are measured separately (I_L, I_R). Measurements are performed at 20 mK in a dilution refrigerator using a standard d.c. transport set-up (see Methods section 'Transport measurements'). An 18-nm layer of HfO_2 dielectric separates the nanowire from seven Ti/Pd bottom gates. Three gates each in the left and right N–S junctions are used to define QDs. The electrochemical potentials in the two QDs, μ_{LD} and μ_{RD}, are controlled by voltages on the respective middle gates, V_{LD} and V_{RD}. Voltage on the central plunger gate, V_{PG}, remains zero for device A and 0.4 V for device B unless mentioned otherwise. An SEM image of device A is shown in Fig. 2a. Characterization of the left and right QDs in device A (Extended Data Fig. 1) shows charging energies of 2.1 meV and 2.75 meV, respectively, much larger than the superconducting gap $\Delta = 270$ μeV in Al. The QDs exhibit irregular Coulomb peak spacings that are typical of the few-electron regime. Transport in the N–QD–S junctions is blocked at energies below Δ, confirming strong suppression of AR. We note that screening due to the presence of multiple metallic gates and a superconducting film in between diminishes cross-coupling between V_{LD} and V_{RD}.

Device fabrication

Our hybrid-nanowire devices are fabricated on pre-patterned substrates, following the shadow-wall lithography technique described in refs. [31,52] and specific details in the supplementary information of ref. [51]. InSb (111) nanowires are deposited onto the substrates using an optical nanomanipulator set-up. For device A, 8 nm of Al was grown at a mix of 15° and 45° angles with respect to the substrate. Subsequently, it was coated with 2 Å of Pt deposited at a 30° angle before capping it with 20 nm evaporated AlO_x. For device B, the same recipe was used with the exception that no Pt coating was deposited. Details of the surface treatment of the nanowires, the growth conditions of the superconductor, the thickness calibration of the Pt coating and the ex-situ fabrication of the ohmic contacts can be found in ref. [51].

Transport measurements

Devices A and B are cooled down in dilution refrigerators with base temperature ~20 mK, equipped with three-dimensional (3D) vector magnets and measured using standard voltage-biased d.c. circuits illustrated in Fig. 1. No lock-in technique is used except in Extended Data Fig. 9. Current amplifier offsets are calibrated using known zero-conductance features when the device is pinched off or in deep Coulomb blockade. Total series resistance in each fridge line is 1.85 kΩ for device A and 2.9 kΩ for device B. Total resistance of the voltage source and current meter is <0.1 kΩ for device A and 102 kΩ for device B, that is, much smaller than the device resistance.

We measured six samples fabricated using similar recipes. Most devices in these samples suffered from shorts between finger gates or between gates and contacts, possibly due to electrostatic discharge. Devices A and B are the only two we have measured with three functional ohmic contacts, at least six functional finger gates and stable gate dielectric, allowing us to define QDs on both sides. Both devices show qualitatively the same behaviour.

Device tune-up

The tuning of our device, in particular the QDs, is done as follows. First, we form a single barrier between N and S by applying a low voltage on the gate closest to S on each side. We then perform local and nonlocal tunnel spectroscopy of the hybrid segment and locate a V_{PG} range in which a hard gap is observed at low energies and extended Andreev bound states are observed at high energy (see Extended Data Fig. 9). Having located a desired value of V_{PG}, we form a second barrier in each junction by applying a lower voltage on the gates closest to the N leads. The confined region between the two barriers thus becomes a QD. We characterize the QDs by measuring its current above the superconducting gap, applying $|V_L|, |V_R| > \Delta/e$ as a function of V_{LD}, V_{RD} and applied magnetic field (see Extended Data Fig. 1c,d). We look for a pair of resonances that correspond to the filling of a single non-degenerate orbital. This is indicated by two resonances separated by only the charging energy at zero field and their linear Zeeman splitting when $B > 0$. We finally measure CAR and ECT between the two QDs (as discussed in Fig. 2). We optimize the measurement by controlling the gates separating the QDs from S to balance low local Andreev current (lowering gate voltage) with high signal-to-noise ratio (raising gate voltage). Having reached a reasonable balance, we again characterize the QDs (Extended Data Fig. 1).

Analysis of the structure of the obtained CAR and ECT patterns

Fitting the data in Fig. 2d,e to a theoretical model[45] (see Supplementary Information) yields QD–QD coupling strengths of the order of electron temperature. Such weak tunnel coupling does not greatly alter the QD eigenstates and allows us to operate QDs as good charge and spin filters. We further notice that finite ECT and CAR currents can be observed when both QDs are within the transport window but not on the diagonal lines dictating energy conservation. Because they appear only on one side of the (anti-)diagonal line corresponding to downhill energy relaxation, these currents result from inelastic processes involving spontaneous emission and are thus non-coherent. We note that the data shown in Fig. 2d,e are taken at different gate settings than the rest of this work and are selected because of high data resolution and Cooper pair splitting efficiency. The (anti-)diagonal resonance line and the strongly (anti-)correlated currents are generic to all QD orbitals that we have investigated.

Role of the Pt layer

Another source for SOC in device A could come from the Pt sub-atomic top layer, although we have not found evidence for this in previous studies[51]. Note that the spin–orbit scattering in Pt is isotropic and cannot give rise to the angular magnetic field dependence. Nevertheless, we have reproduced all the CAR and ECT observations in a second device (device B) where the Pt layer was not included (Extended Data Figs. 6, 7).

Theoretical modelling

See Supplementary Information.

Data availability

Raw data presented in this work and the processing/plotting codes are available at https://zenodo.org/record/5774828.

51. Mazur, G. P. et al. Spin-mixing enhanced proximity effect in aluminum-based superconductor–semiconductor hybrids. *Adv. Mater.* **34**, e2202034 (2022).
52. Borsoi, F. et al. Single-shot fabrication of semiconducting–superconducting nanowire devices. *Adv. Func. Mater.* **31**, 2102388 (2021).
53. Fasth, C., Fuhrer, A., Samuelson, L., Golovach, V. N. & Loss, D. Direct measurement of the spin–orbit interaction in a two-electron InAs nanowire quantum dot. *Phys. Rev. Lett.* **98**, 266801 (2007).

Acknowledgements This work has been supported by the Dutch Organization for Scientific Research (NWO) and Microsoft Corporation Station Q. We also acknowledge a subsidy from Top Consortia for Knowledge and Innovation (TKI toeslag) and support from the European Union's Horizon 2020 research and innovation programme under grant agreement no. 828948, project AndQC. We thank G. de Lange, S. Bergeret, V. Golovach, J. Robinson, M. Aprili, C. Quay, D. Loss and J. Klinovaja for discussions.

Author contributions G.W., G.P.M., N.v.L. and A.B. fabricated the devices. G.W., T.D., S.L.D.t.H. and A.B. performed the electrical measurements. G.W. and T.D. designed the experiment and analysed the data. G.W., T.D. and L.P.K. prepared the manuscript with input from all authors. T.D. and L.P.K. supervised the project. C.-X.L. developed the theoretical model and performed numerical simulation with input from M.W. S.G., G.B. and E.P.A.M.B. performed InSb nanowire growth.

Competing interests The authors declare no competing interests.

Additional information

Supplementary information The online version contains supplementary material available at https://doi.org/10.1038/s41586-022-05352-2.

Correspondence and requests for materials should be addressed to Tom Dvir.

Peer review information *Nature* thanks the anonymous reviewers for their contribution to the peer review of this work. Peer reviewer reports are available.

Reprints and permissions information is available at http://www.nature.com/reprints.

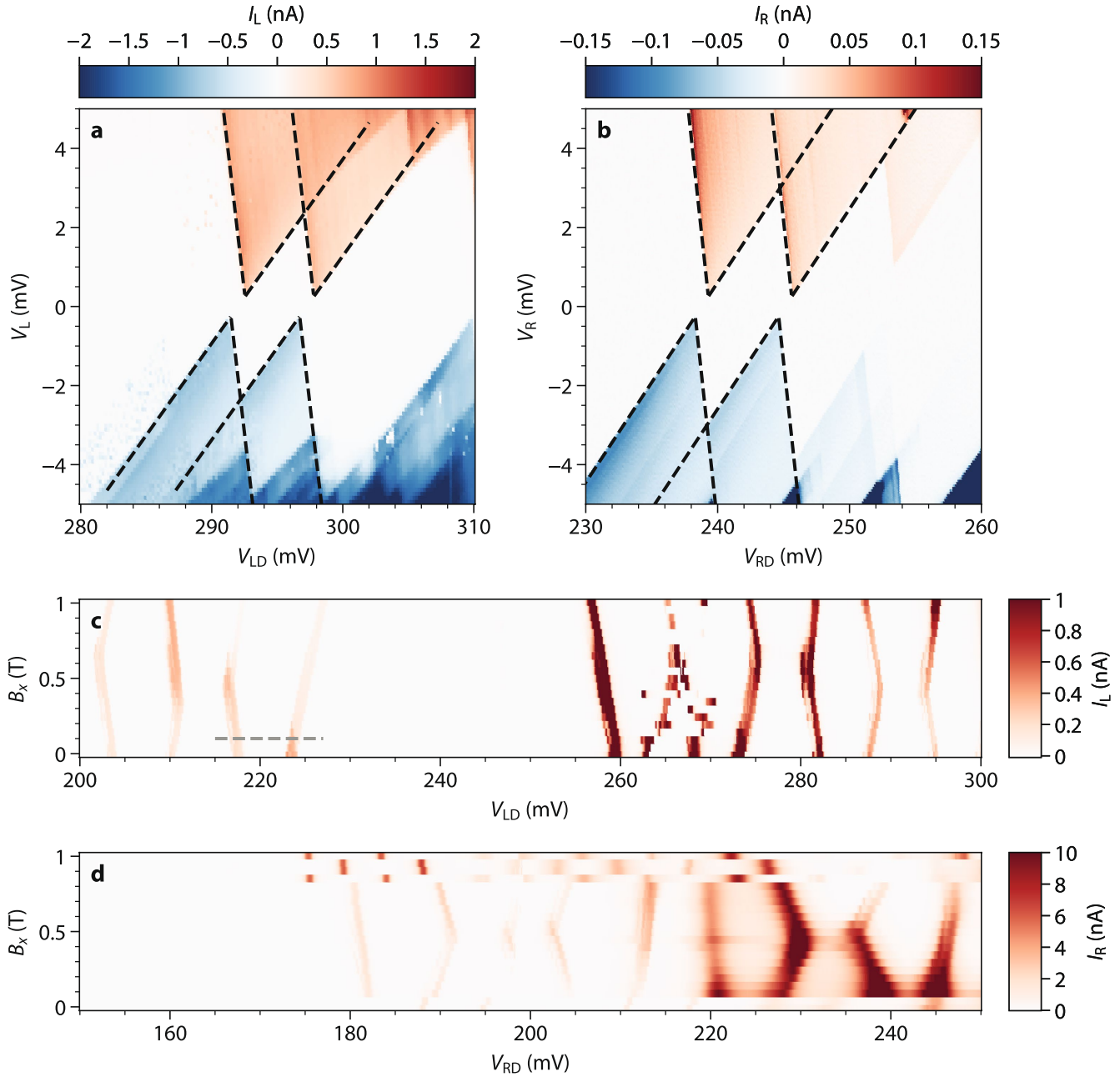

Extended Data Fig. 1 | QD characterization in device A. a, Coulomb blockade diamonds of the left QD. Superimposed dashed lines represent a model with charging energy 2.1 meV, Δ = 250 μV and lever arm 0.4. V_{LD} shown here is different from other measurements of this resonance due to a drift in one tunnel barrier gate during the process of the experiment. **b**, Coulomb blockade diamonds of the right QD. Superimposed dashed lines represent a model with charging energy 2.75 meV, Δ = 250 μV and lever arm 0.435. In both QDs, no subgap current is visible, indicating QDs are weakly coupled to S and retain their charge states. **c**, Current through the left QD at V_L = 500 μV measured against gate voltage and magnetic field along the nanowire, B_x. Spin-degenerate orbitals Zeeman-split in opposite directions while $0 < B_x < 0.5$ T and cross around 0.5 T when Zeeman energy becomes greater than the level spacing ~1.2 meV (see Extended Data Fig. 3 for *g*-factor extraction). The orbital used in Figs. 3, 4 is the pair of resonances marked by grey dashed lines at B = 100 mT. **d**, Current through the right QD at V_R = 500 μV. The orbital used in Figs. 3, 4 is outside the measured range in this plot immediately to the right. All QD resonances we investigated behave similarly including those in Fig. 2, which are selected because of high data resolution and Cooper pair splitting efficiency.

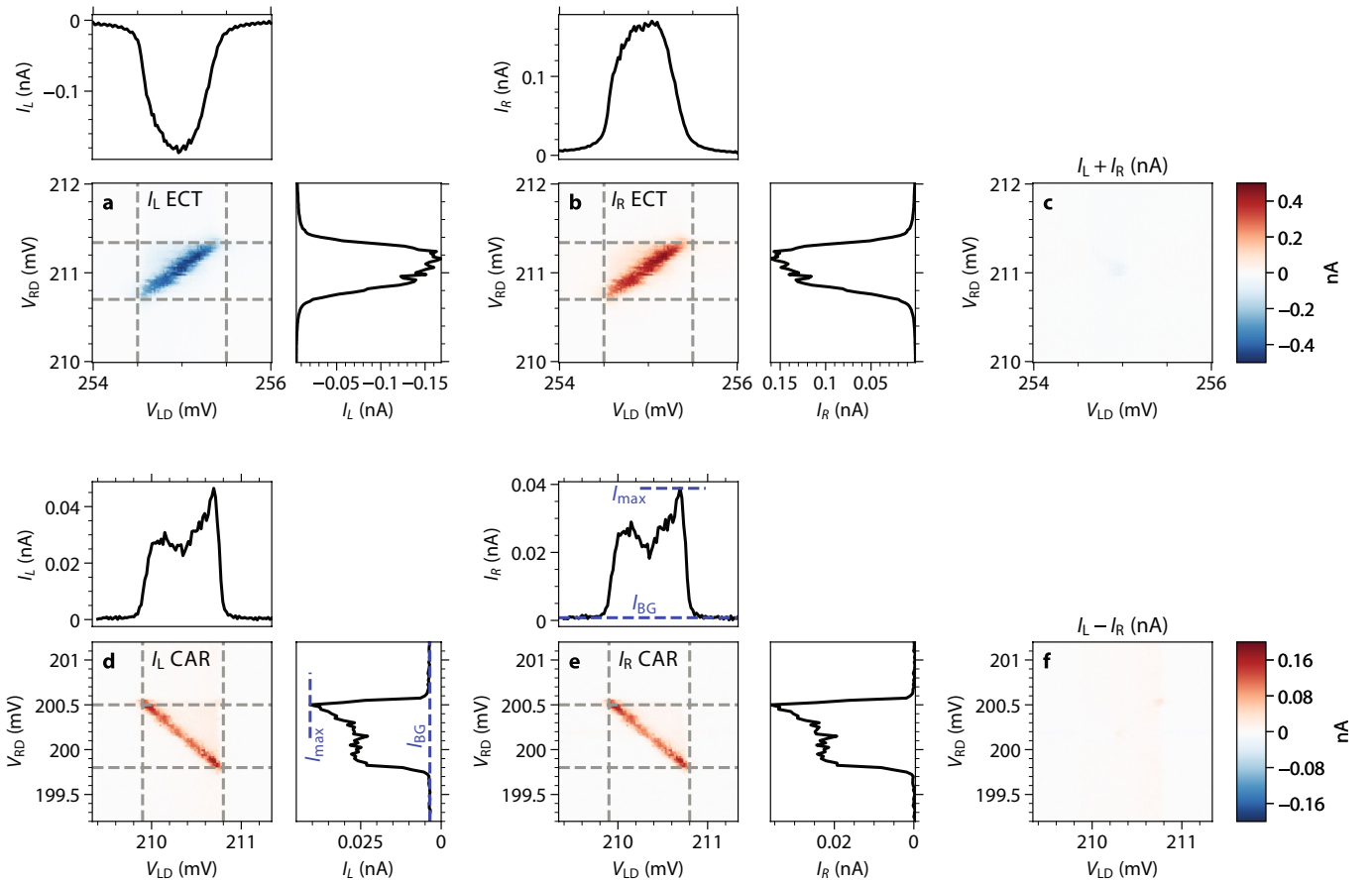

Extended Data Fig. 2 | More analysis on data presented in Fig. 2, including Cooper pair splitting efficiency extraction at $B = 0$. a,**b**, ECT I_L, I_R and averaged currents. Top panel shows signals between the horizontal grey lines averaged over V_{RD}. Right panel shows signals between the vertical grey lines averaged over V_{LD}. Almost no background current is visible unless both dots participate in transport. **c**, $I_L + I_R$ of the ECT measurement is almost 0, verifying $|I_L| = |I_R|$ in most of the phase space except when both QDs are at zero energy and charge selection no longer plays a role. **d**,**e**, CAR I_L, I_R and averaged currents, similar to **a**,**b**. Using $\eta_L \equiv (1 - I_{L,BG}/I_{L,max})$ where the background $I_{L,BG}$ is taken as the average current when V_{RD} is off-resonance and V_{LD} is on-resonance in the right panel of **d**, we obtain a Cooper pair splitting visibility of 91.3% for the left junction. Similarly, the right junction has splitting visibility $\eta_R = 98\%$. This gives combined visibility $\eta_L\eta_R = 89.5\%$. **f**, $I_L - I_R$ of the CAR feature is almost 0, verifying $|I_L| = |I_R|$ except a small amount of local Andreev current in the left QD, manifesting as a vertical feature independent of V_{RD} near $V_{LD} = 210.8$ mV.

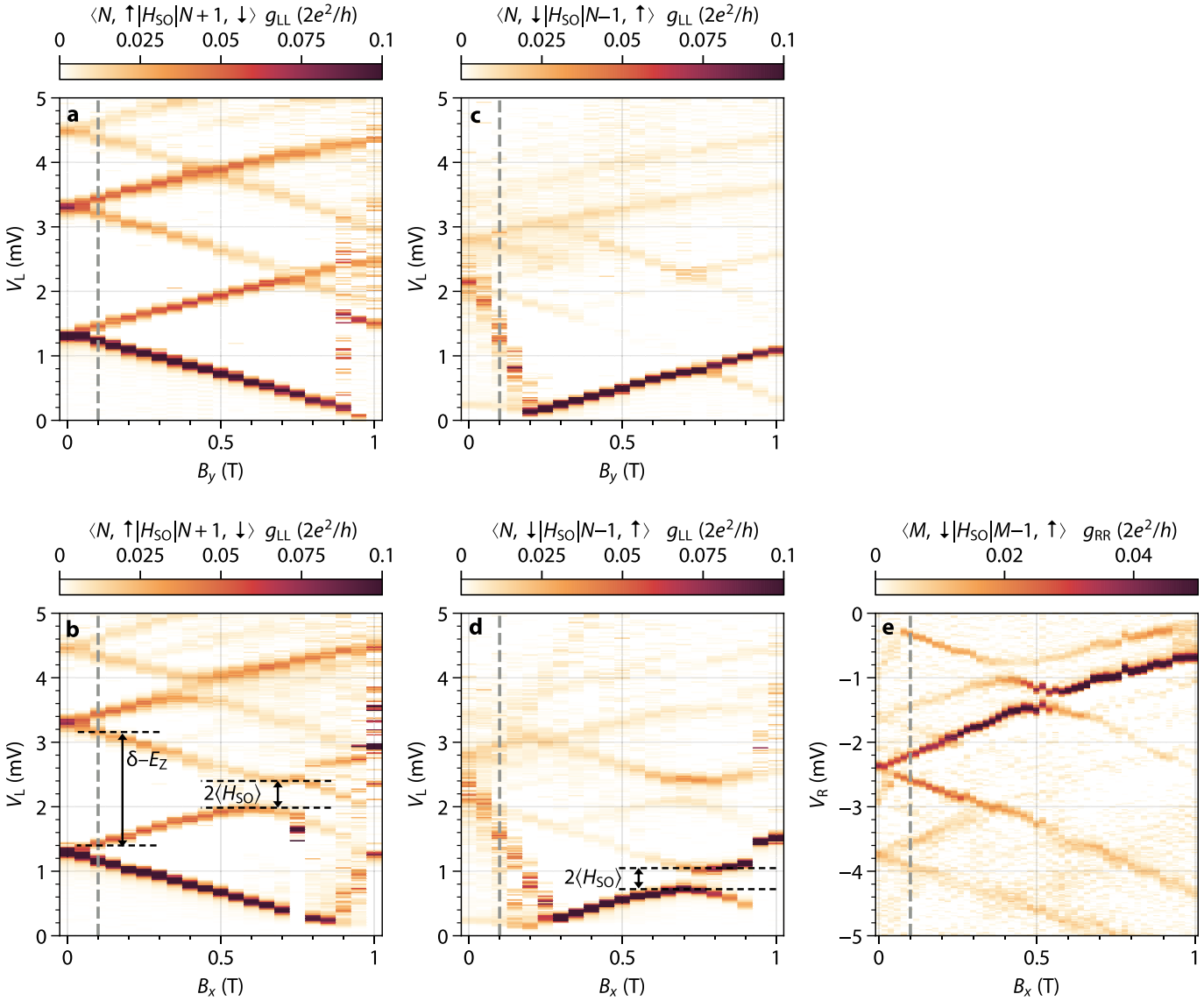

Extended Data Fig. 3 | QD excitation spectra measured using methods previously described[53], from which we extract QD *g*-factor, level spacing and SOC. a,**b**, Left QD excitation spectra evolving under *B* applied along *y* (**a**) and *x* (**b**) for the spin-up ground state. Grey lines mark the field value at which the data in the main text are taken. The observation that opposite-spin excited states cross each other in **a** means spin is conserved, implying B_{so} in the QD and *B* point along the same direction, that is, *y*. Opposite-spin states in **b**, by contrast, anti-cross due to SOC. The quantities needed to calculate the opposite-spin admixture weight (level spacing δ, Zeeman splitting E_z and spin–orbit level repulsion gap $2\langle H_{so}\rangle$ can be directly read from **b** (see Supplementary Information for details). **b** shows the largest value of spin–orbit level repulsion that we have measured in the QDs, which is used as an upper-bound estimation for the effect of SOC in QD in Supplementary Information. The Zeeman-splitting slopes yield $g = 45$, that is, Zeeman energy $g\mu_B B = 260$ μeV at $B = 100$ mT. **c**,**d**, Left QD excitation spectra under *B* along *y* and *x* for the spin-down ground state. The *g*-factor and level spacing are similar to those in **a**,**b** (as seen in data above 0.3 T) but the spin–orbit level repulsion is smaller. **e**. Right QD excitation spectrum under *B* along *x* for the spin-up ground state. Anti-crossings of similar widths to **d** can be observed, although interpretation of the spectrum lines is less clear. No good data could be obtained for the *y* direction and the spin-down ground state. d*I*/d*V* in all panels is calculated by taking the numerical derivative after applying a Savitzky–Golay filter of window length 5 and polynomial order 1 to the measured current. The measurements shown here were conducted using different QD orbitals than those used in Figs. 3, 4. The obtained magnitude of the SOC should be taken as an estimate rather than a precise value.

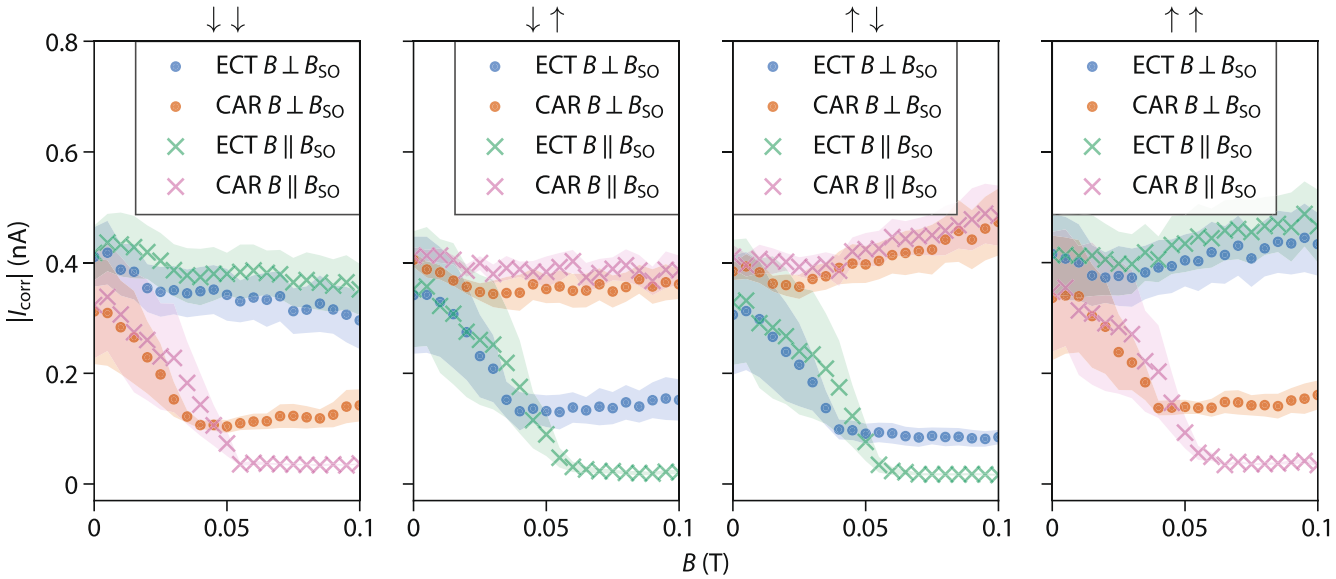

Extended Data Fig. 4 | *B* dependence of CAR and ECT amplitudes of device A. Measurements of CAR and ECT at 4 × 4 spin and bias combinations similar to those in Fig. 4g are performed as functions of B, both when $B = B_y \| B_{SO}$ and when $B = B_x \perp B_{SO}$. At around $|B| = 50$ mT, Zeeman energy exceeds the applied bias voltage of 100 μV and transport across QDs becomes spin polarized. The equal-spin CAR and opposite-spin ECT amplitudes no longer substantially depend on $|B|$ at higher fields.

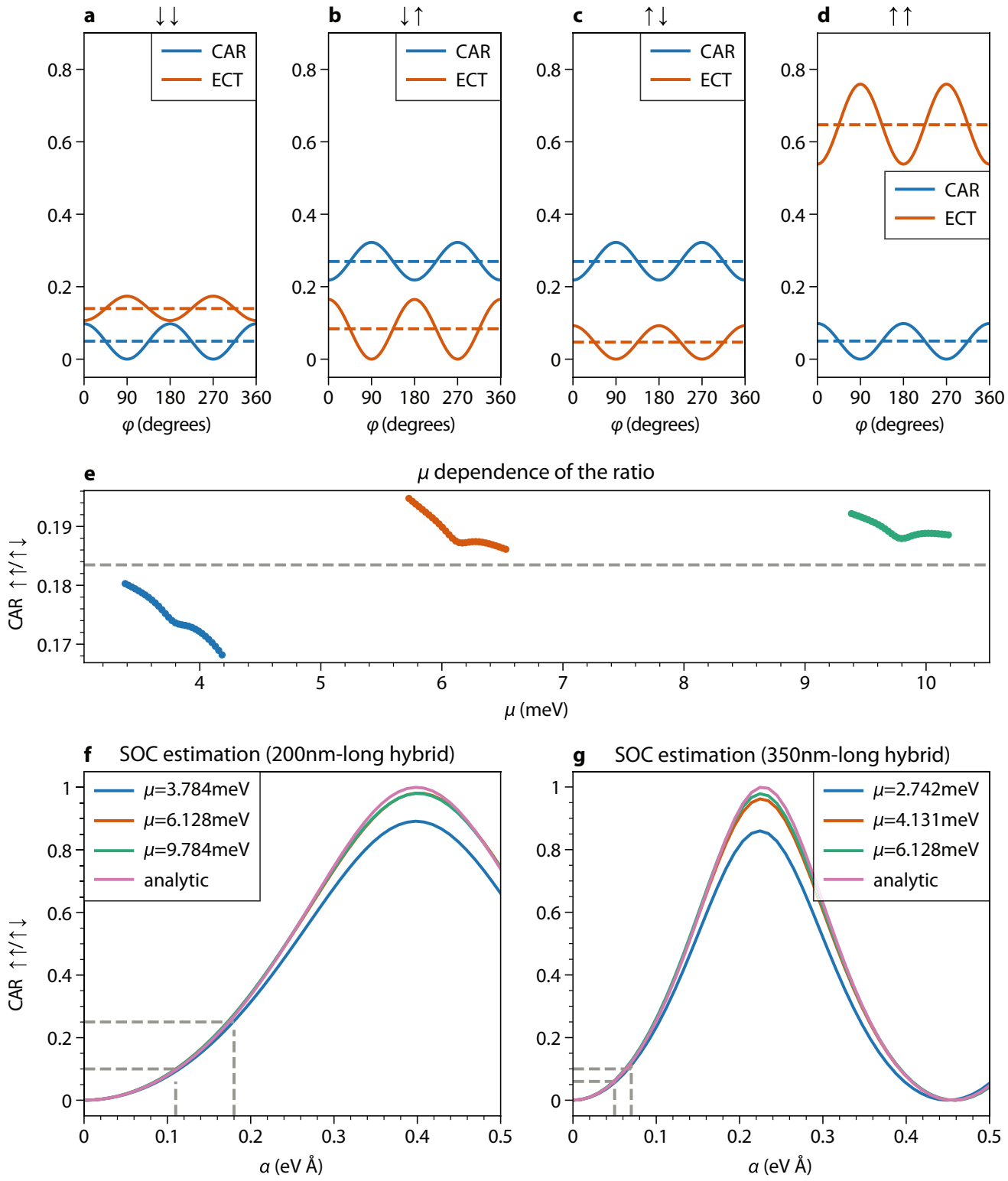

Extended Data Fig. 5 | See next page for caption.

Extended Data Fig. 5 | Theoretical calculations of CAR and ECT amplitudes at finite B, from which we extract the SOC strength in the hybrid segment. See Supplementary Information and ref. [45] for details. **a**–**d**, CAR and ECT amplitudes (proportional to currents) at hybrid-segment $\mu = 6.3$ meV for the four spin combinations when B is rotated in-plane. Dashed lines are the average of each curve. The ratio between ↑↑ CAR to ↑↓ CAR is taken as a proxy of the triplet spin component over singlet in the following panels. **e**, Numerical (solid) and analytical (dashed) calculations of angle-averaged ↑↑/↑↓ CAR ratio are shown in the vicinity of three quantized levels in the hybrid segment (see Supplementary Information and ref. [45] for details). Variation is small throughout the numerically investigated ranges and all are close to the analytical result, signalling that the triplet component estimation is insensitive to the exact chemical potential assumed in the theory. **f**, Dependence of the triplet component on the SOC strength α for a length as in device A (200 nm), numerically calculated at three representative chemical potentials together with the analytical result. In Fig. 4g, triplet/singlet ratios defined here range from ~0.1 to ~0.25. This puts the estimation of α in the range of 0.11 to 0.18 eV Å, in agreement with reported values in literature (0.1 to 0.2 eV Å)[46,47]. **g**, Dependence of the triplet component on the SOC strength α for a length as in device B (350 nm), numerically calculated at three representative chemical potentials together with the analytical result. Similar comparison with data in Extended Data Fig. 6 yields estimations of α in the range of 0.05 to 0.07 eV Å. The weaker SOC could be attributed to the higher V_{PG} used here (0.4 V for device B compared to 0 V for device A) weakening the inversion-symmetry-breaking electric field.

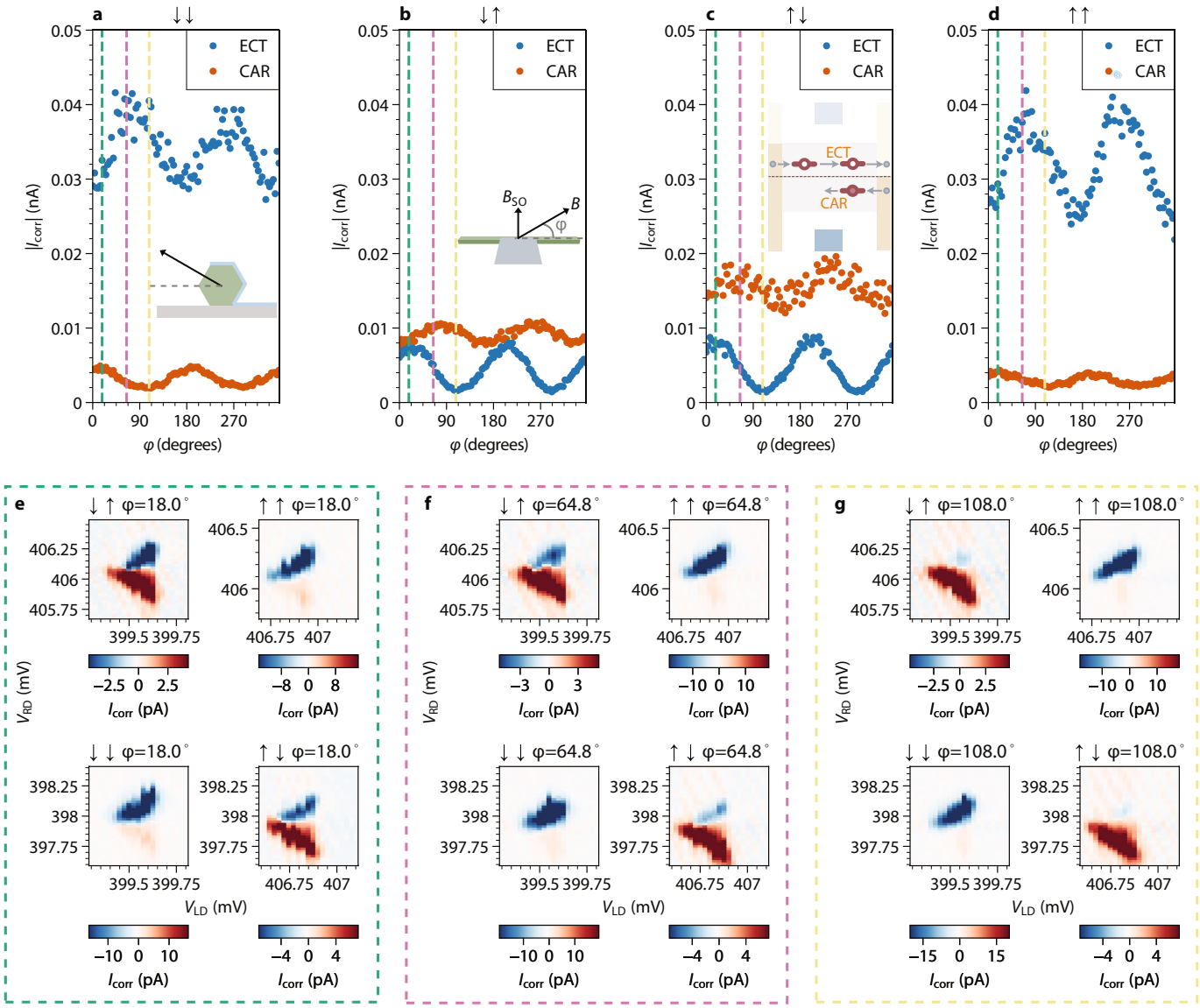

Extended Data Fig. 6 | Anisotropic CAR and ECT reproduced in device B. Device B is fabricated similarly except for the absence of the Pt layer to exclude it as a possible spin-flipping mechanism in the nanowire. **a**–**d**, CAR and ECT amplitudes for four spin combinations when rotating $|B| = 80$ mT in the plane spanned by the nanowire axis and B_{SO} (defined as the direction where equal-spin CAR and opposite-spin ECT are maximally suppressed). The B_{SO} in this device points approximately 30° out of plane (insets: cross-section in **a** and top view in **b**). Inset in **c**: a sketch of the type of bias voltage configurations used in this measurement and in Fig. 4g; see caption of the lower panels for details. **e**–**g**, Selected views of I_{corr} at three representative angles (marked with boxes of the corresponding colour as dashed lines in **a**–**d**). These measurements are performed at $V_L = 70$ μV, $V_R = 0$ because the right QD allows considerable local Andreev current at finite bias due to one malfunctioning gate. This measurement scheme, which is also employed in Fig. 4g, allows us to measure both ECT and CAR without changing the bias. Inset in **c** illustrates when CAR and ECT processes occur using $V_L < V_R = 0$ as an example. Following the same analysis in Fig. 1, we measure ECT when $-eV_L < \mu_{LD} = \mu_{RD} < 0$ and CAR when $-eV_L < \mu_{LD} < 0 < \mu_{RD} = -\mu_{LD} < eV_L$. The main features of the main text data can be reproduced, including anti-diagonal CAR and diagonal ECT lines, strong suppression of opposite-spin ECT and equal-spin CAR along one fixed direction, and their appearance in perpendicular directions.

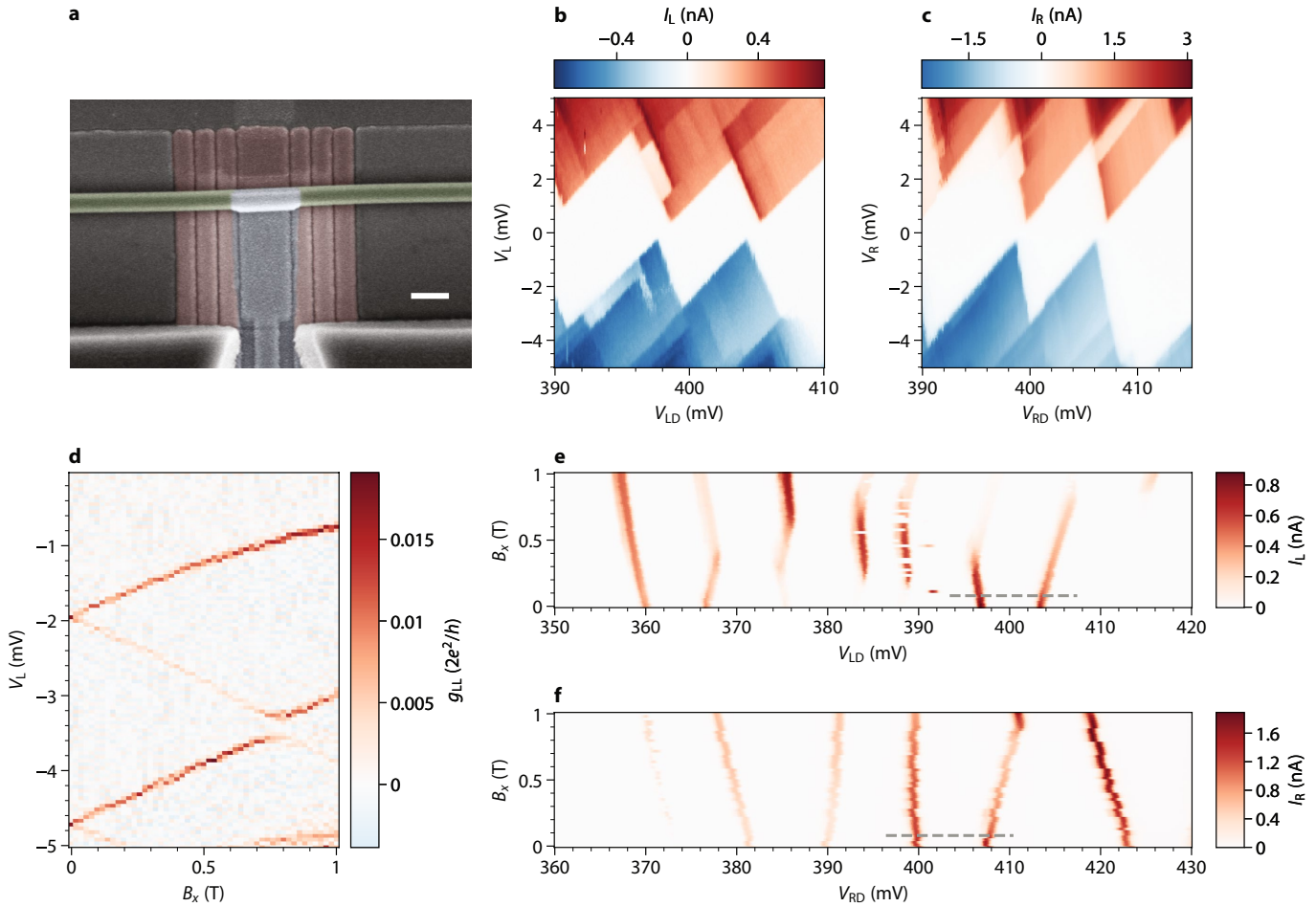

Extended Data Fig. 7 | Device B characterization. a, False-colour SEM image of device B prior to the fabrication of N leads. Green is nanowire, blue is Al and red are the bottom gates. Scale bar is 200 nm. The hybrid segment is 350 nm long. **b**,**c**, QD diamonds of the levels used on both sides at $B = 0$. **d**, Left QD bias spectroscopy under applied $B = B_x$ and $V_{LD} = 357$ mV along the nanowire axis. Level spacing 2.7 meV, g-factor 61 and spin–orbit anti-crossing $2\langle H_{SO}\rangle = 0.25$ meV can be extracted from this plot. dI/dV in this panel is calculated by taking the numerical derivative of the measured current. **e**,**f**, Left and right QD levels evolving under finite B_x. The levels used for taking the data in Extended Data Fig. 6 and the field at which they are taken are indicated by grey dashed lines. g-factor is estimated to be 26 for the right QD.

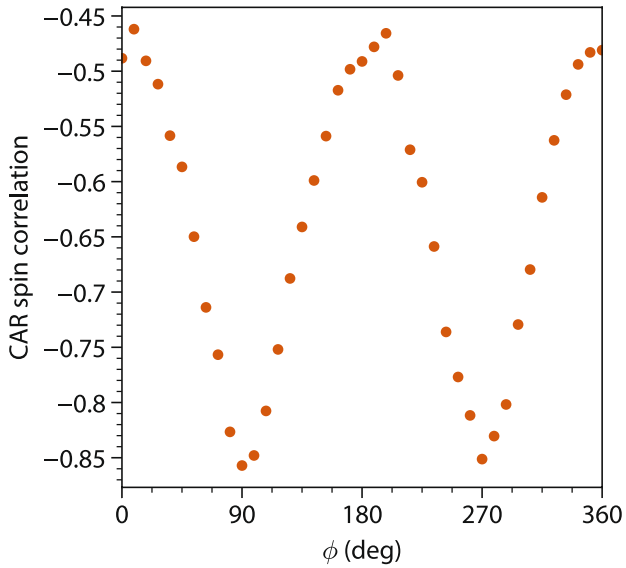

Extended Data Fig. 8 | Spin correlation analysis of the data in Fig. 4g. We define $CAR^{\uparrow\uparrow} \equiv (|I_{corr}|)$ for the ↑↑ spin configuration and similarly for the others, as defined in Fig. 4g. The spin correlation for a given B direction is calculated as $(CAR^{\uparrow\uparrow} + CAR^{\downarrow\downarrow} - CAR^{\uparrow\downarrow} - CAR^{\downarrow\uparrow})/(CAR^{\uparrow\uparrow} + CAR^{\downarrow\downarrow} + CAR^{\uparrow\downarrow} + CAR^{\downarrow\uparrow})$. Perfectly singlet pairing yields −1 spin correlation. The −0.86 correlation when $B \| B_{so}$ is limited by the measurement noise level and can be improved by more signal averaging or more sophisticated analysis methods that are less sensitive to noise. When B points along other directions, the spin anti-correlation reduces as expected for non-singlet pairing.

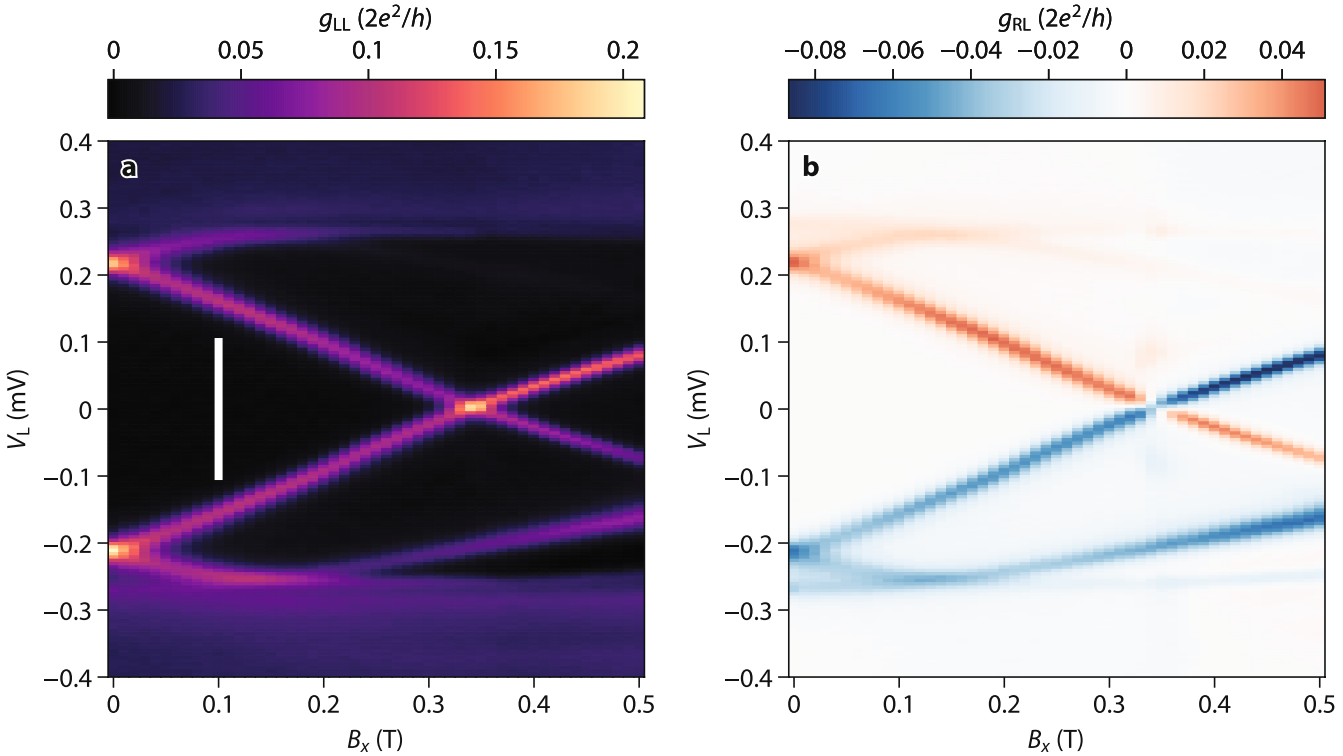

Extended Data Fig. 9 | *B* dependence of the energy spectrum in the middle hybrid segment of device A revealing a discrete Andreev bound state. **a**, $g_{LL} \equiv dI_L/dV_L$. White line indicates the bias range in which the experiments at finite *B* field were performed: the QD energies are kept below the lowest-lying excitation of the middle hybrid segment at all times to avoid sequential tunnelling into and out of it. The *g*-factor of the superconducting–semiconducting hybrid state is seen to be 21 from this plot, smaller than that in QDs. **b**, $g_{RL} \equiv dI_R/dV_L$. The presence of nonlocal conductance corresponding to this state proves this is an extended Andreev bound state (ABS) residing under the entire hybrid segment, tunnel-coupled to both sides. We note that this is the same dataset presented in another manuscript[51] (reproduced under the terms of the CC-BY Creative Commons Attribution 4.0 International license (https://creativecommons.org/licenses/by/4.0); copyright 2022, the authors, published by Wiley-VCH) where it is argued that the observed Zeeman splitting of this ABS also rules out the possibility of the Pt top layer randomizing spin inside the InSb nanowire.

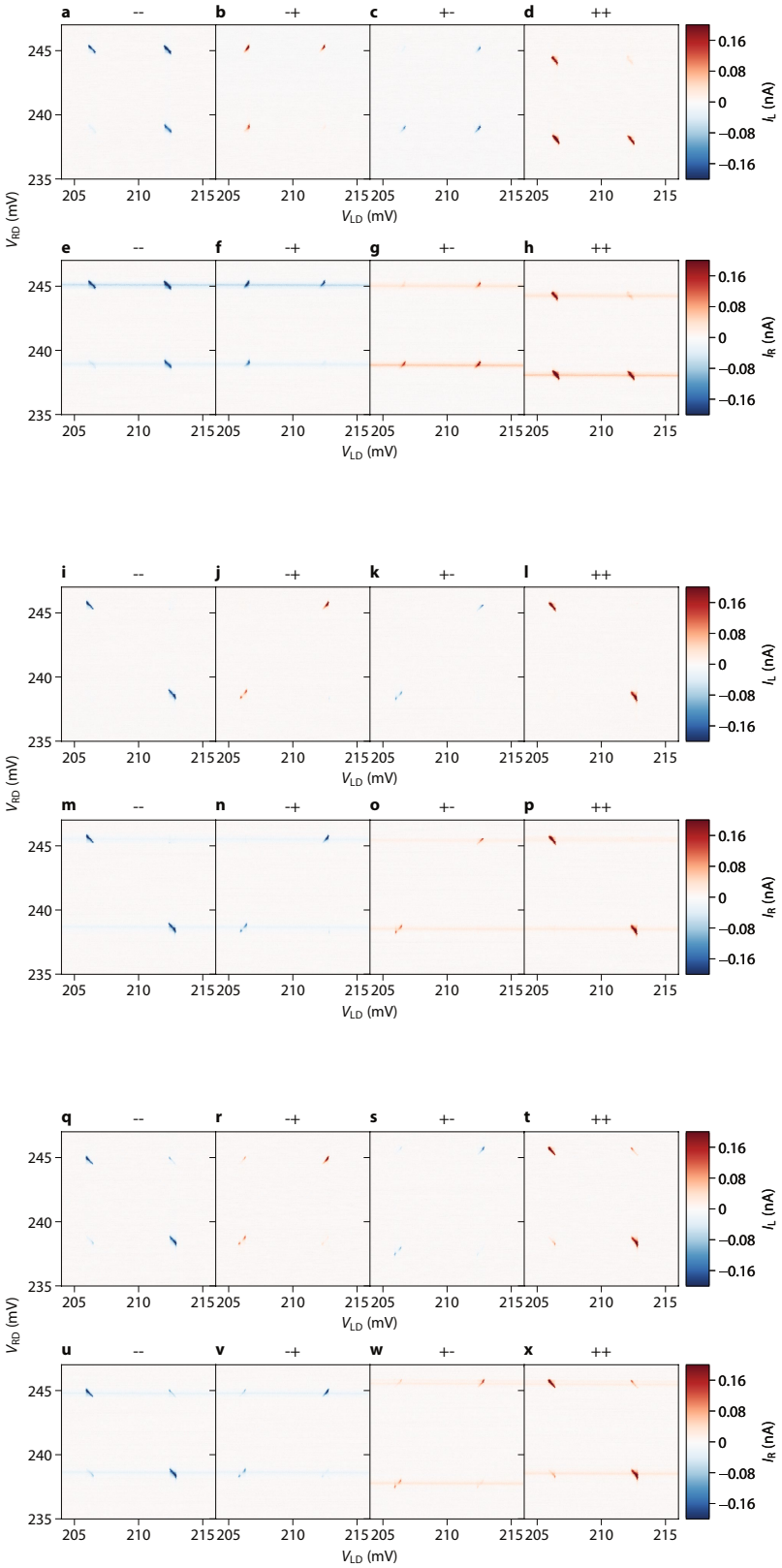

Extended Data Fig. 10 | Plotting of raw data used in Fig. 3 and Fig. 4c,f. For other raw data, see the affiliated data repository (section 'Data availability'). **a**–**h**, I_L, I_R spanning the four joint charge degeneracies and under four N bias polarities at $B = 0$. Figure 3a, for example, is obtained by taking data from **c** and **g** and calculating their geometric mean at each pixel. The horizontal lines in I_R are due to local Andreev processes carried only by the right junction. Since $I_L = 0$ away from the joint charge degeneracies, these purely local currents do not appear in I_{corr}. **i**–**p**, I_L, I_R spanning the four joint charge degeneracies and under four N bias configurations at $B = B_y = 100$ mT. **q**–**x**, I_L, I_R spanning the four joint charge degeneracies and under four N bias configurations at $B = B_x = 100$ mT.